Appl. Sci. **2014**, *4*, 28-41; doi:10.3390/app4010028

OPEN ACCESS

applied sciences

ISSN 2076-3417

www.mdpi.com/journal/applsci

Article

Terahertz Optoelectronic Property of Graphene: Substrate-Induced Effects on Plasmonic Characteristics

I-Tan Lin [1], Yi-Ping Lai [1], Kuang-Hsiung Wu [2] and Jia-Ming Liu [1,*]

[1] Electrical Engineering Department, University of California, Los Angeles, Los Angeles, CA 90095, USA; E-Mails: itanlin@ucla.edu (I-T.L.); yiping@ucla.edu (Y.-P.L.)

[2] Department of Electrophysics, National Chiao-Tung University, Hsinchu 300, Taiwan; E-Mail: khwu@cc.nctu.edu.tw

* Author to whom correspondence should be addressed; E-Mail: liu@ee.ucla.edu; Tel.: +1-310-206-2097; Fax: +1-310-206-4685.

Received: 27 December 2013; in revised form: 22 January 2014 / Accepted: 7 February 2014 / Published: 20 February 2014

Abstract: The terahertz plasmon dispersion of a multilayer system consisting of graphene on dielectric and/or plasma thin layers is systematically investigated. We show that graphene plasmons can couple with other quasiparticles such as phonons and plasmons of the substrate; the characteristics of the plasmon dispersion of graphene are dramatically modified by the presence of the coupling effect. The resultant plasmon dispersion of the multilayer system is a strong function of the physical parameters of the spacer and the substrate, signifying the importance of the substrate selection in constructing graphene-based plasmonic devices.

Keywords: graphene; plasmon; coupling; phonon; scattering rate; optical conductivity; terahertz; Drude model

1. Introduction

Graphene is a two-dimensional layer of carbon atoms in a honeycomb lattice. This unique atomic arrangement results in a linear energy-momentum dispersion of carriers in graphene and an ultrahigh carrier mobility exceeding 200,000 cm^2/V at room temperature [1]. This ultrahigh mobility also implies a long propagation distance of graphene surface plasmons, which are quasiparticles arising from the quantized collective oscillations of the charged carriers on the graphene surface.

These quasiparticles can be excited with the assistance of a grating structure, such as graphene nanoribbons [2–4], a dielectric grating [5,6], or a metal grating [7,8]. Surface plasmons can also be induced near the grain boundary [9], or generated through the interaction with metal particles [10] or sound waves [11]. Besides these momentum-transfer techniques, electron-energy-loss spectroscopy [12,13] and near-field microscopy [14] are also used for the study of graphene surface plasmons. The excited surface plasmons have frequencies in the terahertz (THz) and far-infrared spectral regions. The wave number q of a graphene surface plasmon is proportional to the square of its frequency ω, *i.e.*, $q \propto \omega^2$, when q is much smaller than the Fermi wave number ($q << k_F$); correspondingly, q^{-1} is much smaller than the physical dimension of the graphene structure. This simple relation can be altered by the presence of other quasiparticles, such as surface phonons of a polar substrate [3,12], or plasmons of a metal substrate or another adjacent graphene layer [7,10,15–19]. In this paper, we show that the coupling strength and the deviation from the $q \propto \omega^2$ relation can be described by a simple analytical model, regardless of the type of quasiparticles being coupled.

This paper is organized as follows. In Section 2, we discuss the primary scattering sources and express the scattering rate as a function of the carrier energy and the Fermi energy. Once the scattering rate is determined, the optical conductivity in the THz and far-infrared spectral regions can be obtained, which is discussed in Section 3. In Section 4, we use the derived optical conductivity along with the coupling model to show the plasmon dispersion of graphene on various substrates. The characteristics of the plasmon dispersion are discussed in terms of the distance between the substrate and the graphene layer, the substrate thickness, and other physical parameters of the system. The conclusion is presented in Section 5.

2. Scattering Rate

2.1. Elastic Scattering

Many scattering mechanisms have been suggested for the explanation of the experimental observation [1,20–25]. Among all possible scattering channels, phonon scattering is the intrinsic scattering mechanism that serves as the lower bound of the scattering rate that fundamentally limits the mobility of carriers in graphene. Two types of phonon scattering mechanisms are considered in this paper for carrier transport in graphene: elastic acoustic phonon scattering and inelastic optical phonon scattering; the former is discussed in this section and the latter is discussed in Subsection 2.2. The scattering rate arising from the longitudinal acoustic phonon scattering is given by [26]

$$\tau_{ac}^{-1}(E) = \frac{1}{\hbar^3} \frac{k_B T}{4 v_F^{\,2}} \frac{D_A^{\,2}}{\rho v_{ph}^{\,2}} E \tag{1}$$

where E is the energy of charged carriers, $\hbar$ is the reduced Planck constant, k_B is the Boltzmann constant, T is the temperature, v_F ($\cong 10^6$ m/s) is the Fermi velocity of carriers in graphene, D_A is the acoustic deformation potential, $\rho = 7.6 \times 10^{-7}$ kg/m^2 is the density of graphene per layer, and $v_{ph} = 2 \times 10^4$ m/s is the phonon velocity of the longitudinal acoustic mode [27]. In this paper, $D_A = 18$ eV is assumed, as measured in the experiments [22,25,26,28].

The impurity scattering due to the charged impurity is also considered in the literature for carrier transport in graphene [20,21,23]. For a monolayer graphene sandwiched between two media of different permittivities ε_1 and ε_2, the average dielectric permittivity of such a system is $\varepsilon_{\text{avg}} = (\varepsilon_1 + \varepsilon_2)/2$. The elastic scattering rate arising from the charged impurity scattering can then be written as [29]

$$\tau_{\text{imp}}^{-1}(E) = \frac{n_{\text{i}}}{4\pi\hbar}\frac{E}{(\hbar v_{\text{F}})^2}\int_0^{2\pi} d\theta \frac{\tilde{V}^2}{(1+q_{\text{s}}/q)^2}(1-\cos^2\theta) \tag{2}$$

Where n_{i} is the impurity density, q is the scattering wave number, $\tilde{V} = e^2/2\varepsilon_{\text{avg}}q$ is the Fourier transform of the 2D potential energy, and q_{s} is the screening wave number. With $q = 2k\sin(\theta/2)$, where k is the wave number of carriers and θ is the scattering angle, we obtain the analytical expression for the impurity scattering rate in the limit of $k >> q_{\text{s}}$:

$$\tau_{\text{imp}}^{-1}(E) = \frac{n_{\text{i}}}{4\hbar}\frac{1}{E}\left(\frac{e^2}{2\varepsilon_{\text{avg}}}\right)^2 \tag{3}$$

In fact, q_{s} is a function of both temperature T and wave number q. In this paper, we consider the case of a Fermi energy $E_{\text{f}} >> k_{\text{B}}T$ and a wave number $q \le 2k_{\text{F}}$. Within this limit, q_{s} is approximately the Thomas-Fermi screening wave number given by $e^2\rho(E_{\text{F}})/2\varepsilon_{\text{avg}}$, where $\rho(E_{\text{F}}) = 2E_{\text{F}}/\pi(\hbar v_{\text{F}})^2$ is the density of states at the Fermi energy [29].

2.2. Inelastic Scattering

Using Maxwell's equations and appropriate boundary conditions, a surface optical phonon (SP) mode can be solved for a planar interface between two semi-infinite dielectrics with one dielectric characterized by a transverse optical (TO) frequency [30]. This SP mode has a frequency slightly higher than the associated TO mode; it can efficiently couple with electrons of graphene if the graphene layer is close enough to the polar substrate [31,32]. The SP scattering rate $\tau_{\text{sp}}^{-1}(E)$ contributed by various SP modes v with the phonon energy $\hbar\omega_v$ is approximately given by [33]

$$\tau_{\text{sp}}^{-1}(E) = \sum_v \tau_{\text{sp},v}^{-1}(E) = \frac{e^2}{4\hbar^2 v_{\text{F}}^2}\sum_{v,\pm}\frac{F_v^2\omega_v N_v^{\pm}e^{-2qd}}{q(1+q_{\text{s}}/q)^2}\frac{1-f_0(E\mp\hbar\omega_v)}{1-f_0(E)}\left|\frac{E}{\hbar\omega_v}\mp 1\right| \tag{4}$$

where the scattering wave number is $q = \sqrt{\omega_v^2/v_{\text{F}}^2 - 2E(\pm\hbar\omega_v - E)/\hbar^2 v_{\text{F}}^2}$, with ± standing for the phonon emission (plus sign) and absorption (minus sign) in the scattering process; e is the electronic charge; $N_v^{\pm} = (\exp(\hbar\omega_v/k_{\text{B}}T)-1)^{-1} + 0.5 \pm 0.5$ is the equilibrium phonon occupation number of the surface phonon mode v; d is the spacing between the graphene layer and the substrate; $f_0(E) = \{\exp[(E-\mu)/k_{\text{B}}T]+1\}^{-1}$ is the Fermi–Dirac function, with μ being the chemical potential; F_v is the electron-phonon coupling parameter given by [31,34]

$$F_v^2 = \frac{\hbar\omega_v}{2}\left(\frac{1}{\varepsilon_{\text{high}}+\varepsilon_0} - \frac{1}{\varepsilon_{\text{low}}+\varepsilon_0}\right) \tag{5}$$

where $\varepsilon_{\text{high}}$ and ε_{low} are the high-frequency and low-frequency dielectric permittivities of the polar substrate, respectively, and ε_0 is the permittivity of free space. Equation (4) is a good approximation of $\tau_{\text{sp}}^{-1}(E)$ if the phonon energy $\hbar\omega_v$ is small. For large phonon energies, each term in the summation of Equation (4) has to be multiplied by a correction factor $c_v = 1 + 0.0027\hbar\omega_v$, where $\hbar\omega_v$ is in the unit of meV [33].

Besides the aforementioned extrinsic inelastic SP scattering, there is also intrinsic inelastic scattering, *i.e.*, optical phonons scattering, in graphene. Among various optical phonon modes, the ZO mode at the Brillouin zone center ($\Gamma - \text{ZO}$) has the lowest phonon energy (110 meV) and therefore the highest phonon occupation number [35]. Because the $\Gamma - \text{ZO}$ mode is out-of-plane vibrations, its coupling with in-plane conduction electrons is weak. By comparison, degenerated $\Gamma - \text{LO}$ and $\Gamma - \text{TO}$ modes can efficiently couple with conduction electrons [36], but at room temperature their contributions to the scattering rate is limited because these modes are energetic (200 meV). The TO mode at the zone boundary ($\text{K} - \text{TO}$) has a lower energy around 160 meV; it is therefore suggested to have the highest efficiency in coupling with electrons [37]. However, as we previously showed theoretically [33], the SP modes have a higher coupling efficiency than the $\text{K} - \text{TO}$ mode, which is also confirmed experimentally [22]. Therefore, in this paper, we only consider the surface optical phonon scattering as the dominant inelastic scattering mechanism. The $\text{K} - \text{TO}$ phonon scattering becomes important when graphene is deposited on a substrate such as SiC or *h*-BN where the surface optical phonon scattering is inefficient.

The scattering rate $\tau^{-1}(E) = \tau_{\text{ac}}^{-1}(E) + \tau_{\text{imp}}^{-1}(E) + \tau_{\text{sp}}^{-1}(E)$ as a function of the carrier energy calculated from Equations (1), (3), and (4) for graphene in the air at a distance of $d = 0.34\,\text{nm}$ above a semi-infinite SiO_2 substrate is shown in Figure 1a. The physical parameters of graphene used in the calculation are $E_{\text{F}} \cong \mu = 100\,\text{meV}$, $T = 300\,\text{K}$, and charged impurity density $n_{\text{i}} = 4.4\times10^{11}\,\text{cm}^{-2}$ on the same order of magnitude as the carrier density given by k_{F}^2/π, where $k_{\text{F}} = E_{\text{F}}/\hbar v_{\text{F}}$. The physical parameters of SiO_2 for the calculation of $\tau_{\text{sp}}^{-1}(E)$ can be found in Reference [32]. As can be seen from the data plotted in Figure 1a, $\tau_{\text{imp}}^{-1}(E)$ contributes the most to the total scattering rate. For carriers of large carrier energy *E*, $\tau_{\text{imp}}^{-1}(E)$ decreases with increasing *E*, approaching the behavior described by Equation (3). The second important scattering mechanism is $\tau_{\text{sp}}^{-1}(E)$, which is contributed by two surface phonon modes $\hbar\omega_1$ and $\hbar\omega_2$ of SiO_2. The overall $\tau_{\text{sp}}^{-1}(E)$ increases with *E* mostly due to the fact that the density of states increases with the carrier energy. Most notably $\tau_{\text{sp}}^{-1}(E)$ begins to increase rapidly for $E > \hbar\omega_2 \cong 156\,\text{meV}$, which marks the onset of the intraband phonon emission of $\hbar\omega_2$.

The scattering rate $\tau^{-1}(E_{\text{F}})$ contributed by different scattering mechanisms as a function of E_{F} is shown in Figure 1b. To better see the dependence of the scattering rate on E_{F}, the curves in Figure 1b are normalized to $\tau^{-1}(E_{\text{F}})$ and are shown in Figure 1c. As can be seen, the relative weight of phonon scattering increases due to the increase of the density of states with E_{F}. By contrast, $\tau_{\text{imp}}^{-1}(E_{\text{F}})$ decreases with E_{F} because of the enhanced screening by the increasing carrier density $n = \sqrt{\pi E_{\text{F}}/\hbar v_{\text{F}}}$.

Figure 1. Scattering rate of carriers in graphene as a function of (**a**) the carrier energy; and (**b**) the Fermi energy. Curves from top to bottom: the total scattering rate $\tau^{-1} = \tau_{ac}^{-1} + \tau_{imp}^{-1} + \tau_{sp}^{-1}$ (blue curves), $\tau_{imp}^{-1} + \tau_{sp}^{-1}$ (red curves), and τ_{imp}^{-1} (black curves). Curves plotted in (**c**) are scattering rates plotted in (**b**) but normalized to the total scattering rate.

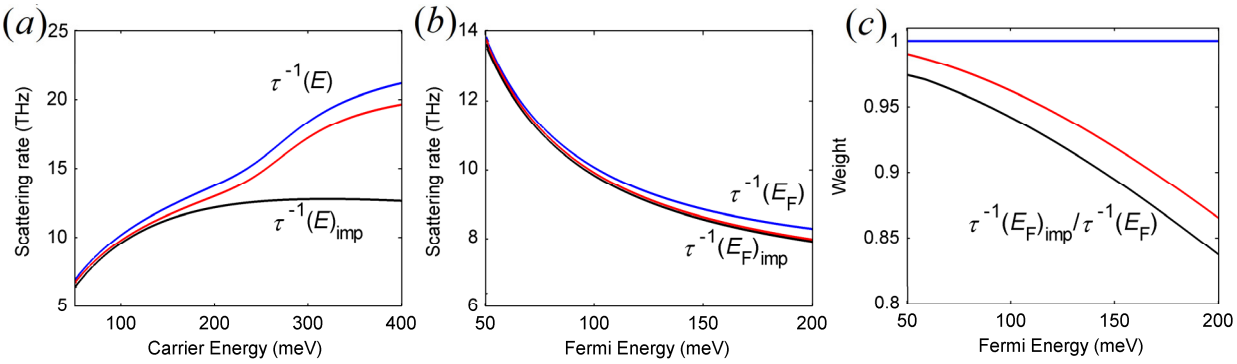

3. Optical Conductivity

3.1. Drude Model

Semiclassically, the optical conductivity of monolayer graphene can be described by [29,38]

$$\sigma(\omega) = -\frac{e^2}{\pi\hbar^2}\int_{-\infty}^{\infty} dE \frac{|E|}{\tau^{-1}(E) - i\omega}\frac{df_0(E)}{dE} \tag{6}$$

where ω is the angular frequency of the electric field. Because the behavior of $\tau^{-1}(E)$ is complicated, as we have shown in Figure 1a, the analytical solution to Equation (6) is difficult to obtain. Alternatively, we can replace $\tau^{-1}(E)$ in Equation (6) with an effective energy-independent but frequency-dependent scattering rate $\tau_{eff}^{-1}(\omega)$ to obtain an analytical expression [33]:

$$\sigma(\omega) = \frac{e^2}{\pi\hbar^2}\frac{2k_BT}{\tau_{eff}^{-1}(\omega) - i\omega}\ln\left[2\cosh\left(\frac{\mu}{2k_BT}\right)\right] \tag{7}$$

It can be shown that if $\mu >> k_BT$, $\tau_{eff}^{-1}(\omega) \cong \tau^{-1}(E_F)$ and Equation (7) becomes the familiar simple Drude model $\sigma_0/(1 - i\omega\tau_{eff})$ with $\sigma_0 = e^2E_F\tau_{eff}/\pi\hbar^2$, which is commonly used in fitting the experimental data. If the condition $\mu >> k_BT$ is not valid, $\tau_{eff}^{-1}(\omega)$ has to be calculated numerically. Nevertheless, with $E_F \geq 100\,\text{meV}$ and $T = 300\,\text{K}$, it has been shown that $\tau_{eff}^{-1}(\omega)$ is a weak function of frequency, and $\tau_{eff}^{-1}(\omega) \cong \tau^{-1}(E_F)$ is a fairly good approximation for Equation (7) [33].

3.2. RPA Model

In the Drude model, the nonlocal effect is ignored. To describe the organized oscillation of electrons due to the long-range nature of Coulomb force among them, the Drude model is insufficient when the oscillation is characterized by a large wave number q. To account for the nonlocality, the optical conductivity of graphene as a function of both ω and q can be derived within the random phase

approximation (RPA). In the RPA, the out-of-phase response of electrons to the external field is assumed to average out to zero due to the random location of the electrons in a large quantity [39].

The polarizability of graphene within the RPA is given as [40]

$$\Pi(q,\omega) = -\frac{4}{A}\sum_{\mathbf{k}ss'} \frac{f(sE_{\mathbf{k}}) - f(s'E_{\mathbf{k}'})}{\hbar\omega + sE_{\mathbf{k}} - s'E_{\mathbf{k}'} + \mathrm{i}\delta} \frac{1 + ss'\cos\theta}{2} \tag{8}$$

where A is the area of graphene, s and s' denote the band indices having the values of 1 for the conduction band or -1 for the valance band, δ is an infinitesimal number, $\mathbf{k}' = \mathbf{k} + \mathbf{q}$, θ is the scattering angle between $\mathbf{k}$ and $\mathbf{k}'$, and $E_{\mathbf{k}} = \hbar v_{\mathrm{F}} |\mathbf{k}|$. The analytical expression for Equation (8) has previously been obtained in the limit of $\mu >> k_{\mathrm{B}}T$ [40,41] and in the collisionless limit of $\tau^{-1} \to 0$. To account for the finite scattering rate, we replace ω with $\omega_\gamma = \omega + i\tau^{-1}(E_{\mathrm{F}})$ in Equation (8) and follow the same procedure as the one in References [40,41] assuming $\mu >> k_{\mathrm{B}}T$; the result is

$$\Pi(q,\omega) = \frac{2k_{\mathrm{F}}}{\pi v_{\mathrm{F}}\hbar} - \frac{q^2}{4\pi\hbar\sqrt{\omega_\gamma^{\,2} - v_{\mathrm{F}}^{\,2}q^2}} \left[G\left(\frac{2k_{\mathrm{F}}v_{\mathrm{F}} + \omega_\gamma}{v_{\mathrm{F}}q}\right) + \mathrm{sgn}(\omega - 2k_{\mathrm{F}}v_{\mathrm{F}}) G\left(\frac{2k_{\mathrm{F}}v_{\mathrm{F}} - \omega_\gamma}{v_{\mathrm{F}}q}\right) \right] \tag{9}$$

where $G(x) = x\sqrt{x^2 - 1} - \ln\left(x + \sqrt{x^2 - 1}\right)$; $\mathrm{sgn}(x) = 1$ if $x \geq 0$ and -1 otherwise. Equation (9) is identical to Equation (7) of Reference [42] in a slightly different form. Apparently, by setting $\tau^{-1}(E_{\mathrm{F}}) \to 0$ for $\omega_\gamma \to \omega$, Equation (9) reduces to the collisionless results in References [40,41]. To comply with local electron conservation, Equation (9) needs to be modified to [43,44]

$$\Pi_\gamma(q,\omega) = \frac{\omega_\gamma}{\omega\Pi(q,\omega)^{-1} + \mathrm{i}\tau^{-1}(E_{\mathrm{F}})\Pi(q,0)^{-1}} \tag{10}$$

where $\Pi(q,\omega)$ is given by Equation (9) and $\Pi(q,0)$ is obtained by setting both $\tau^{-1}(E_{\mathrm{F}})$ and ω to zero in Equation (9). Equation (10) is called the RPA relaxation time (RPA-RT) approximation, which properly accounts for the finite scattering rate and the conservation of local electrons [44].

The optical conductivity within the RPA-RT approximation is given by

$$\sigma_{\mathrm{RPA}}(q,\omega) = -\mathrm{i}\omega\frac{e^2}{q^2}\Pi_\gamma(q,\omega) \tag{11}$$

The optical conductivity obtained from the Drude model and that from the RPA-RT approach in the long-wavelength limit ($q \to 0$) are plotted in Figure 2. As can be seen in Figure 2a, the RPA-RT result, σ_{RPA}, is almost identical to the Drude result in the region $\hbar\omega << \mu$. By contrast, in the high-frequency region where $\hbar\omega$ is comparable to 2μ, the Drude model fails to account for the interband transition, whereas the RPA-RT results properly account for it, as seen in Figure 2b. Due to the simplicity of the Drude model, in this paper we use Equation (7) for the conductivity of graphene. The RPA-RT conductivity, given by Equation (11), is calculated to show that the obtained results using the Drude model are good approximations in the low-energy region.

Figure 2. Optical conductivity of graphene for (a) $\hbar\omega \le \mu$, and (b) $\hbar\omega \ge \mu$. The solid curves are derived from the Drude model (Equation (7)), and the dashed curves are obtained using the RPA-RT approach (Equation (11)). The real part and the imaginary part of the optical conductivity are plotted in red and black colors, respectively. For both figures, the parameters used are $T = 300$ K, $\mu = 100$ meV, and $\tau^{-1}(E_F) = 10$ THz.

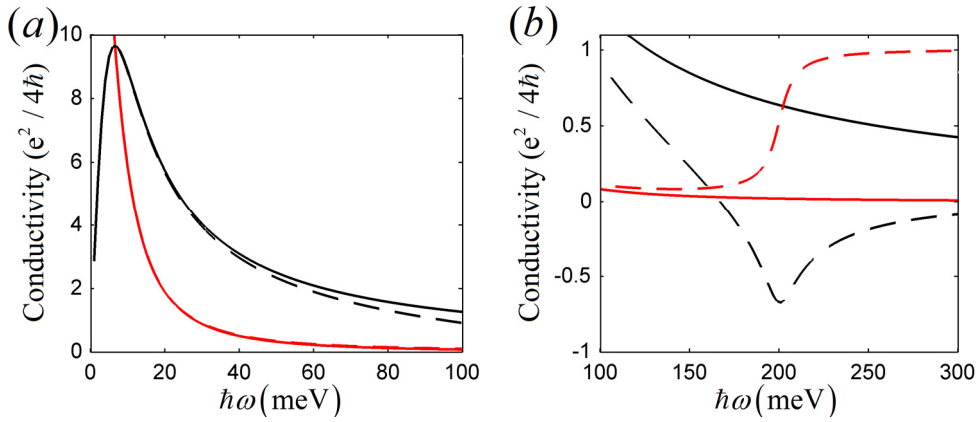

4. Plasmon Dispersion

The plasmon dispersion of graphene sandwiched between air and a substrate of a constant permittivity ε_{sub} is well known [40,43,45]. The physical structure is illustrated in Figure 3a. Using Maxwell's equations with appropriate boundary conditions, the plasmon dispersion can be obtained by solving the equation:

$$\varepsilon_{ave} + i\frac{q}{2\omega}\sigma(q,\omega) = 0 \tag{12}$$

where $\varepsilon_{ave} = (\varepsilon_{sub} + \varepsilon_0)/2$. Because of the finite scattering rate, $q = q_1 + iq_2$ has to be a complex number with $q_2 \neq 0$ for Equation (12) to be valid. In Equation (12) and below, we have ignored the retardation effect in view of the fact that the speed of light c in vacuum is 300 time higher than the Fermi velocity of graphene. As a result, $\omega/q_1 << c$ is generally true as we shall see in the following figures for the plasmon dispersion of graphene on various substrates. The region where the retardation effect is important, *i.e.*, ω/q_1 is comparable to c, is indistinguishable from the $\hbar\omega$ axis, and thus is not considered in this paper.

Jablan *et al.* [43] have shown that as long as $q_2 << q_1$ and $\hbar\omega << 2E_F$, the Drude model is sufficient to determine the plasmon dispersion described by Equation (12) without the need of the RPA-RT approach. By plugging Equation (7) in Equation (12), we obtain

$$q_1^{-1} = \frac{e^2 k_B T}{\varepsilon_{ave}\omega^2 \pi\hbar^2} \ln\left[2\cosh\left(\frac{\mu}{2kT}\right)\right] \tag{13}$$

$$q_2^{-1} = \frac{e^2 k_B T\tau}{\varepsilon_{ave}\omega\pi\hbar^2} \ln\left[2\cosh\left(\frac{\mu}{2kT}\right)\right] \tag{14}$$

where τ is the inverse of $\tau^{-1}(E_F)$. Because $2\pi q_1^{-1}$ is the wavelength of the plasmons and q_2^{-1} represents the distance of propagation for the plasmonic field amplitude to decrease to $1/e$ of its

original amplitude, it is meaningful to define $q_2^{-1}/q_1^{-1}=\tau\omega$ as a figure of merit. Clearly, regarding surface plasmons in terms of q_2^{-1}/q_1^{-1}, a high frequency is preferred for graphene, whereas for a metal, q_2^{-1}/q_1^{-1} decreases with increasing frequency in the optical region [46]. Note that τ is also a function of frequency [33]. For a frequency ω that is too large, above either 48 THz or $\hbar\omega>2E_F$, the optical phonon scattering or the interband scattering becomes important; then, τ decreases and therefore q_2^{-1}/q_1^{-1} might decrease with increasing frequency.

The plasmon dispersion of graphene can be greatly altered by coupling graphene plasmons with other quasiparticles. Both theoretically and experimentally, it has been shown that graphene plasmons can couple with surface phonons of polar substrates [3,12], and with plasmon modes of metal particles or a metal surface [7,10,15]. Coupled plasmon modes resulted from the coupling of two graphene layers have also been studied [16–19,47]. Coupled plasmon modes of these systems can be determined from the following equation when the retardation effect is ignored [15]:

$$\frac{1}{\varepsilon_2}\frac{\varepsilon_1+\varepsilon_{sub}\tanh qd_{sub}}{\Gamma+\tanh qd_2}+\frac{1}{\varepsilon_{sub}}\frac{\varepsilon_{sub}+\varepsilon_1\tanh qd_{sub}}{1+\Gamma\tanh qd_2}=0 \tag{15}$$

where d_{sub} is the thickness of the substrate that has the permittivity ε_{sub}, d_2 is the thickness of the spacer between the graphene layer and the substrate, $\Gamma=(\varepsilon_0+i\sigma q/\omega)/\varepsilon_2$, and ε_1, ε_2, ε_0 are respectively the permittivity of the medium below the substrate, the permittivity of the spacer, and the permittivity of free space above the graphene layer, as shown in Figure 3b,c. In the case of double-layer graphene, as shown in Figure 3d, Equation (15) is reduced by setting $d_1\to 0$. In the following, we thoroughly study the coupled plasmon dispersion of these systems while considering the existence of a finite scattering rate of carriers in graphene.

Figure 3. Structures considered in this paper: (**a**) graphene on a semi-infinite substrate of a constant permittivity; (**b**) graphene on a polar substrate; (**c**) graphene on a metal substrate; and (**d**) double-layer graphene. The substrate is characterized by a permittivity of ε_{sub} and a thickness of d_{sub}. The spacer between the graphene layer and the substrate is characterized by a permittivity of ε_2 and a thickness of d_2. Below the substrate is a semi-infinite dielectric medium that has a permittivity of ε_1.

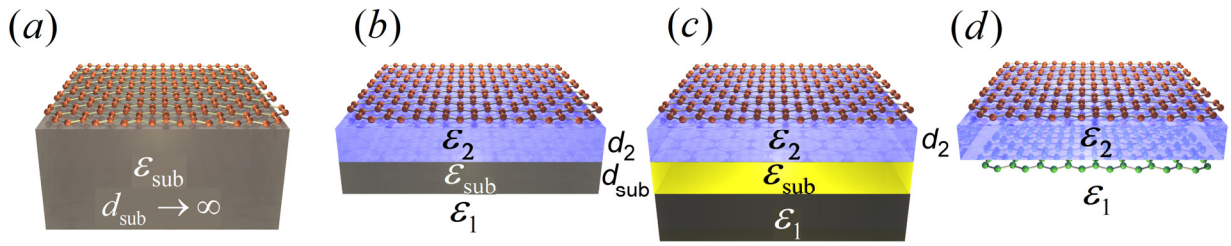

4.1. Graphene on a Polar Substrate

Consider a graphene layer at a distance d_2 above a polar substrate, as shown in Figure 3b. The polar substrate is characterized by a permittivity given by

$$\varepsilon_{\text{sub}} = \varepsilon_{\text{high}} + \left(\varepsilon_{\text{int}} - \varepsilon_{\text{high}}\right)\frac{\omega_{\text{TO2}}^{\ 2}}{\omega_{\text{TO2}}^{\ 2} - \omega^2} + \left(\varepsilon_{\text{low}} - \varepsilon_{\text{int}}\right)\frac{\omega_{\text{TO1}}^{\ 2}}{\omega_{\text{TO1}}^{\ 2} - \omega^2} \tag{16}$$

where ω_{TO1} and ω_{TO2} are the two lowest TO frequencies of the substrate with $\omega_{\text{TO2}} > \omega_{\text{TO1}}$, and ε_{int} is the intermediate permittivity for frequency ω between the two TO frequencies, $\omega_{\text{TO2}} > \omega > \omega_{\text{TO1}}$. These parameters for different materials can be found in Reference [32]. Using Equations (7), (15), and (16), the coupled plasmon-phonon dispersion of graphene at a distance d_2 above a SiO_2 substrate is shown in Figure 4a, where q is normalized to $k_{\text{F}} = E_{\text{F}} / \hbar v_{\text{F}}$, and $E_{\text{F}} \cong \mu = 100$ meV is used; the scattering rare is chosen to be 10 THz as a reasonable value given in Figure 1b. As can be seen, the dispersion of the coupled plasmon mode deviates from the decoupled mode given by Equation (12) with $\varepsilon_{\text{ave}} = \left(\varepsilon_2 + \varepsilon_0\right)/2$ (dashed curve). The deviation is especially strong around $\hbar\omega = \hbar\omega_1 \cong 59$ meV where the surface phonon mode is located and the coupling of plasmons and phonons is the strongest. As the distance d_2 between graphene and the substrate increases, the dispersion of the coupled plasmon mode (red curve) approaches that of the decoupled mode. As the thickness of the substrate d_{sub} increases, the effective permittivity ε_{ave} increases as the space otherwise filled by air $\varepsilon_1 = \varepsilon_0$ is now filled with SiO_2. As a consequence, q_1 also increases for the same $\hbar\omega$ (blue curve), as can be told from their relation in Equation (13). Therefore, we see that d_{sub} and d_2 can serve as tuning parameters for shaping the plasmon dispersion.

Figure 4. Plasmon dispersion of graphene on (**a**) SiO_2 and (**b**) various semi-infinite polar substrates ($d_{\text{sub}} \to \infty$). The structure considered is shown in Figure 3b. In all figures, $\varepsilon_1 = \varepsilon_0$, $\varepsilon_2 = 2\varepsilon_0$, $\mu = 100$ meV, and $\tau^{-1} = 10$ THz are used. In (**a**), unless otherwise specified, $d_{\text{sub}} = 50$ nm and $d_2 = 30$ nm are used for the calculation. In (**b**), different materials for the polar substrate are represented by different colors as specified in the legend; $d_2 = 30$ nm is used for the solid curves, and $d_2 \to \infty$ is assumed for the dashed curve. The black curves in (**a**) calculated using the Drude conductivity are plotted again in (**c**) to compare with the dotted curve obtained using the RPA-RT approach. The parameters used for the RPA-RT calculation are $d_{\text{sub}} = 50$ nm and $d_2 = 30$ nm.

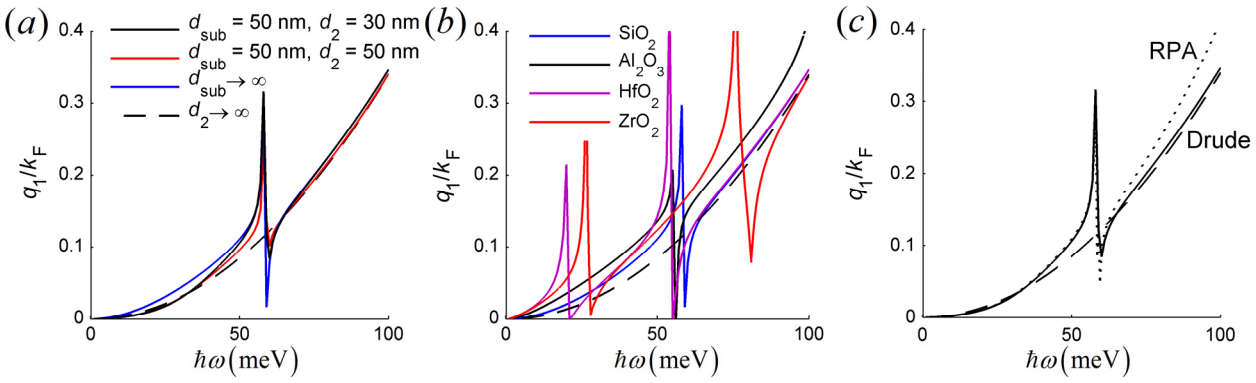

In Figure 4b, we plot the dispersion of the coupled plasmon-phonon mode for graphene at a distance d_2 above a semi-infinite substrate of various materials. As can be seen, some dispersion relations are characterized by two peaks because they are associated with substrates that have two surface phonon modes of energies within the plotted range. Note that as q increases, nonlocal effects become strong, and the results obtained in Figure 4a,b using the Drude conductivity for graphene deviate from the dispersion obtained using σ_{RPA}, as shown in Figure 4c for graphene on SiO_2 with $d_{\mathrm{sub}} = 50\,\mathrm{nm}$ and $d_2 = 30\,\mathrm{nm}$ as an example.

Figure 5. Plasmon dispersion of (**a**) graphene on a gold substrate and (**b**,**c**) double-layer graphene. The related structures are shown in Figure 3c,d. In all figures, $\mu = 100\,\mathrm{meV}$ and $\tau^{-1} = 10\,\mathrm{THz}$ are used for graphene. Thin solid, thick solid, and dashed curves are calculated for $d_2 = 30\,\mathrm{nm}$, $d_2 = 50\,\mathrm{nm}$, and $d_2 \to \infty$, respectively. Black and red curves are calculated for $\varepsilon_2 = 2\varepsilon_0$ and $\varepsilon_2 = \varepsilon_0$, respectively. The dotted curves are obtained using the RPA-RT approach with parameters $d_2 = 30\,\mathrm{nm}$ and $\varepsilon_2 = 2\varepsilon_0$. In (**a**), $d_{\mathrm{sub}} = 50\,\mathrm{nm}$, $\varepsilon_1 = 3.9\varepsilon_0$, $\omega_{\mathrm{p}} = 8.89\,\mathrm{eV}$, and $\gamma = 17\,\mathrm{THz}$ are used. In (**b**,**c**), $\varepsilon_1 = \varepsilon_0$ is assumed. Curves for the same plasmon mode are grouped by an ellipse.

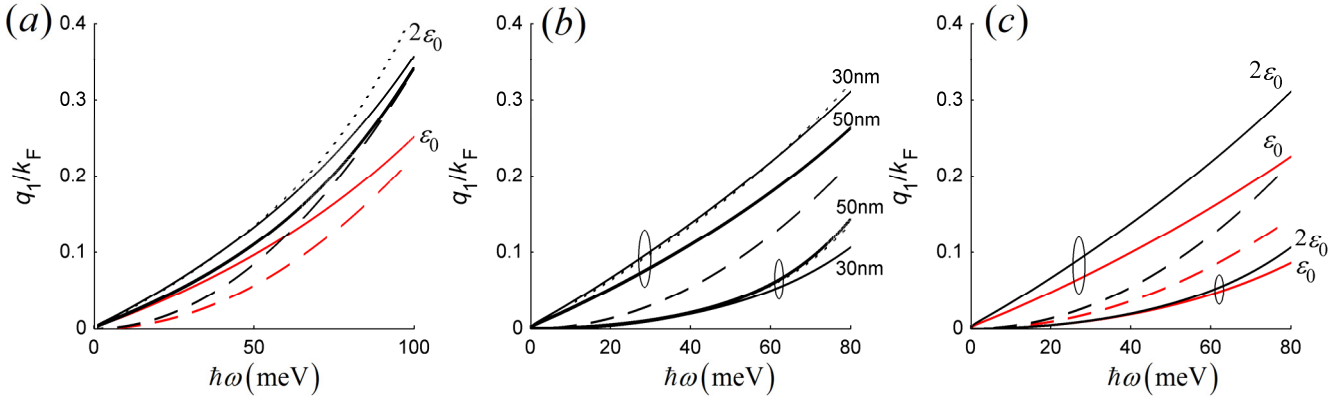

4.2. Graphene on A Metal Substrate

Consider a structure shown in Figure 3c where a monolayer graphene is at a distance d_2 above a metal substrate of a thickness of d_{sub} deposited on a semi-infinite dielectric material. The permittivity of the metal substrate is modeled as

$$\varepsilon_{\mathrm{sub}} = \varepsilon_0\left(1 - \frac{\omega_{\mathrm{p}}^{\,2}}{\omega(\omega + \mathrm{i}\gamma)}\right) \tag{17}$$

where ω_{p} is the bulk plasma frequency and γ is the scattering rate of the metal. Using Equations (7), (15) and (17), the plasmon mode of the system due to the coupling between the graphene layer and the metal slab can be numerically solved, as shown in Figure 5a, where the metal is assumed to be gold with $\omega_{\mathrm{p}} = 8.89\,\mathrm{eV}$ and $\gamma = 17\,\mathrm{THz}$ [48]. As can be seen, by coupling graphene with a metal substrate, the wave number q of the plasmon mode increases. This coupling effect gradually vanishes as d_2 increases. A larger ε_2 (larger $\varepsilon_{\mathrm{avg}}$) also gives a larger q according to Equation (13). However, d_{sub}

and ε_1 have nearly no effect on shaping the plasmon dispersion because d_{sub} is always much larger than the skin depth of gold, which is about $c/\omega_{\text{p}} = 0.22\,\text{nm}$ in the THz frequency region. We also calculated the plasmon dispersion for graphene on different metal substrates; the dispersion curves overlapped and can hardly be distinguished. Therefore, the choice of the metal substrate is not important regarding the plasmon dispersion within the THz frequency region. The plasmon dispersion of the system is also calculated using σ_{PRA} and plotted as the dotted curve in Figure 5a. At high q_1 region, the RPA-RT results start to deviate from the curves obtained using the Drude conductivity. Nevertheless, in the low-q_1 region, the Drude model is sufficiently accurate to describe the plasmon dispersion of the system.

4.3. Double-Layer Graphene

Consider the double-layer graphene shown in Figure 3d with the bottom graphene layer serving as a substrate having the conductivity σ_{sub} and $\varepsilon_1 = \varepsilon_0$. By applying the limit $d_{\text{sub}} \to 0$ and substituting ε_{sub} in Equation (15) with

$$\varepsilon_{\text{sub}} = \text{i}\frac{\sigma_{\text{sub}}}{\omega d_{\text{sub}}} \tag{18}$$

the coupled plasmon modes of double layer graphene can be solved. Note that σ_{sub} does not have to be equal to σ of the upper graphene layer because they do not necessarily have the same E_{F} or τ^{-1}. For simplicity, here we set $\sigma_{\text{sub}} = \sigma$; then with ε_{sub} given by Equation (18), Equation (15) becomes

$$\tanh qd_2 = -\frac{2\Gamma}{\Gamma^2 + 1} \tag{19}$$

which has been derived previously [47]. Equation (19) can also be derived by finding zeros of the linear-response function of the double layer graphene system [15]. The coupled plasmon modes are plotted in Figure 5b,c using Equations (7) and (19). As can be seen, the plasmon dispersion described by Equation (13) is strongly hybridized as the distance between two graphene layers d_2 decreases. We also see that similar to the case of a metal substrate, q_1 increases for the same $\hbar\omega$ as ε_2 increases. In Figure 5b, the plasmon dispersion of the double-layer graphene is also calculated using σ_{PRA} and plotted as the dotted curve. As in the case of graphene on a metal substrate, the Drude model is a good approximation for the plasmon dispersion in the low-q_1 region.

5. Conclusions

In this paper, the plasmon dispersion of graphene on various substrates is systematically investigated. We start from the calculation of the scattering rate and the optical conductivity. Once these physical parameters are known, the plasmon dispersion of a multilayer system consisting of graphene on dielectric and/or plasma thin layers can be determined. We show that the characteristics of the plasmon dispersion are a strong function of the distance between the graphene layer and the substrate, the permittivity of the spacer, the surrounding permittivity, and various physical parameters of the substrate. Our studies show the importance of the substrate selection as well as the

system configuration in designing graphene-based plasmonic optoelectronic devices in the THz frequency region.

Acknowledgments

This work was supported by U.S. Air Force AOARD under Grant Award No. FA2386-13-1-4022.

Conflicts of Interest

The authors declare no conflict of interest.

References

1. Morozov, S.V.; Novoselov, K.S.; Katsnelson, M.I.; Schedin, F.; Elias, D.C.; Jaszczak, J.A.; Geim, A.K. Giant intrinsic carrier mobilities in graphene and its bilayer. *Phys. Rev. Lett.* **2008**, *100*, 016602.
2. Christensen, J.; Manjavacas, A.; Thongrattanasiri, S.; Koppens, F.H.L.; de Abajo, F.J.G. Graphene plasmon waveguiding and hybridization in individual and paired nanoribbons. *ACS Nano* **2011**, *6*, 431–440.
3. Yan, H.; Low, T.; Zhu, W.; Wu, Y.; Freitag, M.; Li, X.; Guinea, F.; Avouris, P.; Xia, F. Damping pathways of mid-infrared plasmons in graphene nanostructures. *Nat. Photonics* **2013**, *7*, 394–399.
4. Ju, L.; Geng, B.; Horng, J.; Girit, C.; Martin, M.; Hao, Z.; Bechtel, H.A.; Liang, X.; Zettl, A.; Shen, Y.R.; *et al*. Graphene plasmonics for tunable terahertz metamaterials. *Nat. Nanotechnol.* **2011**, *6*, 630–634.
5. Zhan, T.R.; Zhao, F.Y.; Hu, X.H.; Liu, X.H.; Zi, J. Band structure of plasmons and optical absorption enhancement in graphene on subwavelength dielectric gratings at infrared frequencies. *Phys. Rev. B* **2012**, *86*, 165416.
6. Bludov, Y.V.; Peres, N.M.R.; Vasilevskiy, M.I. Graphene-based polaritonic crystal. *Phys. Rev. B* **2012**, *85*, 245409.
7. Gu, X.; Lin, I.T.; Liu, J.-M. Extremely confined terahertz surface plasmon-polaritons in graphene-metal structures. *Appl. Phys. Lett.* **2013**, *103*, 071103.
8. Popov, V.V.; Polischuk, O.V.; Davoyan, A.R.; Ryzhii, V.; Otsuji, T.; Shur, M.S. Plasmonic terahertz lasing in an array of graphene nanocavities. *Phys. Rev. B* **2012**, *86*, 195437.
9. Fei, Z.; Rodin, A.S.; Gannett, W.; Dai, S.; Regan, W.; Wagner, M.; Liu, M.K.; McLeod, A.S.; Dominguez, G.; Thiemens, M.; *et al*. Electronic and plasmonic phenomena at graphene grain boundaries. *Nat. Nanotechnol.* **2013**, *8*, 821–825.
10. Niu, J.; Shin, Y.J.; Lee, Y.; Ahn, J.-H.; Yang, H. Graphene induced tunability of the surface plasmon resonance. *Appl. Phys. Lett.* **2012**, *100*, 061116.
11. Farhat, M.; Guenneau, S.; Bağcı, H. Exciting graphene surface plasmon polaritons through light and sound interplay. *Phys. Rev. Lett.* **2013**, *111*, 237404.
12. Liu, Y.; Willis, R.F. Plasmon-phonon strongly coupled mode in epitaxial graphene. *Phys. Rev. B* **2010**, *81*, 081406.

13. Politano, A.; Marino, A.R.; Formoso, V.; Farías, D.; Miranda, R.; Chiarello, G. Evidence for acoustic-like plasmons on epitaxial graphene on Pt(111). *Phys. Rev. B* **2011**, *84*, 033401.
14. Fei, Z.; Andreev, G.O.; Bao, W.; Zhang, L.M.; McLeod, S.A.; Wang, C.; Stewart, M.K.; Zhao, Z.; Dominguez, G.; Thiemens, M.; *et al*. Infrared nanoscopy of dirac plasmons at the graphene–SiO_2 interface. *Nano Lett.* **2011**, *11*, 4701–4705.
15. Lin, I.-T.; Liu, J.-M. Coupled surface plasmon modes of graphene in close proximity to a plasma layer. *Appl. Phys. Lett.* **2013**, *103*, 201104.
16. Wang, B.; Zhang, X.; Yuan, X.; Teng, J. Optical coupling of surface plasmons between graphene sheets. *Appl. Phys. Lett.* **2012**, *100*, 131111.
17. Profumo, R.E.V.; Asgari, R.; Polini, M.; MacDonald, A.H. Double-layer graphene and topological insulator thin-film plasmons. *Phys. Rev. B* **2012**, *85*, 085443.
18. Stauber, T.; Gómez-Santos, G. Plasmons in layered structures including graphene. *New J. Phys.* **2012**, *14*, 105018.
19. Correas-Serrano, D.; Gomez-Diaz, J.S.; Perruisseau-Carrier, J.; Alvarez-Melcon, A. Spatially dispersive graphene single and parallel plate waveguides: Analysis and circuit model. *IEEE Trans. Microw. Theory Tech*. **2013**, *61*, 4333–4344.
20. Hwang, E.H.; Adam, S.; Das Sarma, S. Carrier transport in two-dimensional graphene layers. *Phys. Rev. Lett.* **2007**, *98*, 186806.
21. Chen, J.H.; Jang, C.; Adam, S.; Fuhrer, M.S.; Williams, E.D.; Ishigami, M. Charged-impurity scattering in graphene. *Nat. Phys.* **2008**, *4*, 377–381.
22. Chen, J.-H.; Jang, C.; Xiao, S.; Ishigami, M.; Fuhrer, M.S. Intrinsic and extrinsic performance limits of graphene devices on SiO2. *Nat. Nanotechnol.* **2008**, *3*, 206–209.
23. Tan, Y.W.; Zhang, Y.; Bolotin, K.; Zhao, Y.; Adam, S.; Hwang, E.H.; Das Sarma, S.; Stormer, H.L.; Kim, P. Measurement of scattering rate and minimum conductivity in graphene. *Phys. Rev. Lett.* **2007**, *99*, 246803.
24. Tanabe, S.; Sekine, Y.; Kageshima, H.; Nagase, M.; Hibino, H. Carrier transport mechanism in graphene on SiC(0001). *Phys. Rev. B* **2011**, *84*, 115458.
25. Zou, K.; Hong, X.; Keefer, D.; Zhu, J. Deposition of high-quality HfO_2 on graphene and the effect of remote oxide phonon scattering. *Phys. Rev. Lett.* **2010**, *105*, 126601.
26. Hwang, E.H.; Das Sarma, S. Acoustic phonon scattering limited carrier mobility in two-dimensional extrinsic graphene. *Phys. Rev. B* **2008**, *77*, 115449.
27. Castro, E.V.; Ochoa, H.; Katsnelson, M.I.; Gorbachev, R.V.; Elias, D.C.; Novoselov, K.S.; Geim, A.K.; Guinea, F. Limits on charge carrier mobility in suspended graphene due to flexural phonons. *Phys. Rev. Lett.* **2010**, *105*, 266601.
28. Dean, C.R.; Young, A.F.; Meric, I.; Lee, C.; Wang, L.; Sorgenfrei, S.; Watanabe, K.; Taniguchi, T.; Kim, P.; Shepard, K.L.; *et al*. Boron nitride substrates for high-quality graphene electronics. *Nat. Nanotechnol.* **2010**, *5*, 722–726.
29. Hwang, E.H.; Das Sarma, S. Screening-induced temperature-dependent transport in two-dimensional graphene. *Phys. Rev. B* **2009**, *79*, 165404.
30. Wang, S.Q.; Mahan, G.D. Electron scattering from surface excitations. *Phys. Rev. B* **1972**, *6*, 4517–4524.

31. Konar, A.; Fang, T.; Jena, D. Effect of high-κ gate dielectrics on charge transport in graphene-based field effect transistors. *Phys. Rev. B* **2010**, *82*, 115452.
32. Lin, I.T.; Liu, J.-M. Surface polar optical phonon scattering of carriers in graphene on various substrates. *Appl. Phys. Lett.* **2013**, *103*, 081606.
33. Lin, I.T.; Liu, J.M. Terahertz frequency-dependent carrier scattering rate and mobility of monolayer and AA-stacked multilayer graphene. *IEEE J. Sel. Top. Quantum Electron*. **2014**, *20*, 8400108.
34. Fratini, S.; Guinea, F. Substrate-limited electron dynamics in graphene. *Phys. Rev. B* **2008**, *77*, 195415.
35. Malard, L.M.; Pimenta, M.A.; Dresselhaus, G.; Dresselhaus, M.S. Raman spectroscopy in graphene. *Phys. Rep.* **2009**, *473*, 51–87.
36. Piscanec, S.; Lazzeri, M.; Mauri, F.; Ferrari, A.C.; Robertson, J. Kohn anomalies and electron-phonon interactions in graphite. *Phys. Rev. Lett.* **2004**, *93*, 185503.
37. Yao, Z.; Kane, C.L.; Dekker, C. High-field electrical transport in single-wall carbon nanotubes. *Phys. Rev. Lett.* **2000**, *84*, 2941–2944.
38. Stauber, T.; Peres, N.M.R.; Guinea, F. Electronic transport in graphene: A semiclassical approach including midgap states. *Phys. Rev. B* **2007**, *76*, 205423.
39. Bohm, D.; Pines, D. A collective description of electron interactions. I. magnetic interactions. *Phys. Rev.* **1951**, *82*, 625–634.
40. Hwang, E.H.; Das Sarma, S. Dielectric function, screening, and plasmons in two-dimensional graphene. *Phys. Rev. B* **2007**, *75*, 205418.
41. Wunsch, B.; Stauber, T.; Sols, F.; Guinea, F. Dynamical polarization of graphene at finite doping. *New J. Phys.* **2006**, *8*, 318.
42. Pyatkovskiy, P.K. Dynamical polarization, screening, and plasmons in gapped graphene. *J. Phys. Condens. Matter* **2009**, *21*, 025506.
43. Jablan, M.; Buljan, H.; Soljačić, M. Plasmonics in graphene at infrared frequencies. *Phys. Rev. B* **2009**, *80*, 245435.
44. Mermin, N.D. Lindhard dielectric function in the relaxation-time approximation. *Phys. Rev. B* **1970**, *1*, 2362–2363.
45. Koppens, F.H.L.; Chang, D.E.; de Abajo, F.J.G. Graphene plasmonics: A platform for strong light–matter interactions. *Nano Lett.* **2011**, *11*, 3370–3377.
46. West, P.R.; Ishii, S.; Naik, G.V.; Emani, N.K.; Shalaev, V.M.; Boltasseva, A. Searching for better plasmonic materials. *Laser Photonics Rev.* **2010**, *4*, 795–808.
47. Gan, C.H.; Chu, H.S.; Li, E.P. Synthesis of highly confined surface plasmon modes with doped graphene sheets in the midinfrared and terahertz frequencies. *Phys. Rev. B* **2012**, *85*, 125431.
48. Zeman, E.J.; Schatz, G.C. An accurate electromagnetic theory study of surface enhancement factors for silver, gold, copper, lithium, sodium, aluminum, gallium, indium, zinc, and cadmium. *J. Phys. Chem.* **1987**, *91*, 634–643.